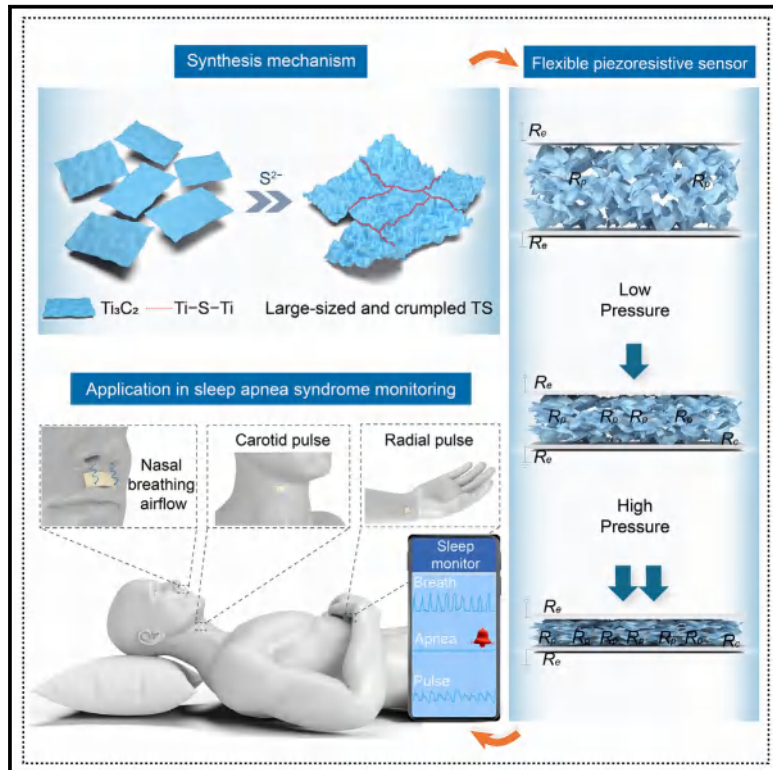


Atomic sulfur-bonded titanium carbide nanosheets for flexible piezoresistive sensor in monitoring sleep apnea syndrome

Graphical abstract



Authors

Yan Bai, Longlu Wang, Xiang Zou, ..., Shujuan Liu, Wei Huang, Qiang Zhao

Correspondence

iamwwzhao@njupt.edu.cn (W.Z.), provost@nwpu.edu.cn (W.H.), iamqzhao@njupt.edu.cn (Q.Z.)

In brief

An atomic sulfur-bonded strategy is innovatively proposed to fabricate large-sized, crumpled, and antioxidative Ti₃C₂/Na₂S (TS) materials for flexible piezoresistive sensors to monitor SAS. It creates a precedent for devising Ti₃C₂-based piezoresistive materials with excellent compression characteristics and rich contact site variation that pave the way for highly sensitive and stable flexible piezoresistive sensors. A wireless respiratory monitoring system utilizing a TS-based flexible piezoresistive sensor provides precise sleep apnea diagnosis and timely health alerts for enhanced patient care.

Highlights

- Atomic sulfur-bonded strategy is proposed for large-sized TS
- Crumpled microstructure of TS demonstrates abundant compression space
- Edge passivation protects TS against oxidation
- Wireless respiratory monitoring system is achieved for high-precision monitoring



Improvement

Enhanced performance with innovative design or material control

Bai et al., 2025, Matter 8, 1927
February 5, 2025 © 2024 Elsevier Inc. All rights reserved, including those for text and data mining, AI training, and similar technologies.
<https://doi.org/10.1016/j.matt.2024.11.021>

Article

Atomic sulfur-bonded titanium carbide nanosheets for flexible piezoresistive sensor in monitoring sleep apnea syndrome

Yan Bai,¹ Longlu Wang,² Xiang Zou,¹ Ning Ding,¹ Yuhui Feng,¹ Zhen You,¹ Weiwei Zhao,^{1,4,*} Weikang Wang,¹ Feifei Lin,¹ Yuzhe Chen,¹ Yijie Zhang,¹ Jianmin Li,² Fangyi Guan,² Shujuan Liu,¹ Wei Huang,^{3,*} and Qiang Zhao^{1,2,*}

¹State Key Laboratory of Organic Electronics and Information Displays & Jiangsu Key Laboratory for Biosensors, Institute of Advanced Materials (IAM), Nanjing University of Posts and Telecommunications, 9 Wenyuan Road, Nanjing 210023, China

²College of Electronic and Optical Engineering & College of Flexible Electronics (Future Technology), Nanjing University of Posts and Telecommunications (NUPT), 9 Wenyuan Road, Nanjing 210023, China

³Frontiers Science Center for Flexible Electronics (FSCFE), MIIT Key Laboratory of Flexible Electronics (KLoFE), Northwestern Polytechnical University, Xi'an 710072, China

⁴Lead contact

*Correspondence: iamwwzhao@njupt.edu.cn (W.Z.), provost@nwpu.edu.cn (W.H.), iamqzhao@njupt.edu.cn (Q.Z.)

<https://doi.org/10.1016/j.matt.2024.11.021>

PROGRESS AND POTENTIAL Flexible sensors have always played an indispensable role in monitoring subtle signals. Confronted with escalating complexities in human health issues, more and more researchers are incorporating flexible sensors into the field of medical health monitoring. Ti_3C_2 is considered a kind of piezoresistive material, but its poor structural compressibility in films and antioxidation restricts its feasibility as an independent piezoresistive material for high-performance pressure sensors. Although combining it with polymers or elastic substrates effectively enhances its elasticity, introducing insulating materials can impede the detection of subtle pressures and reduce sensitivity. We propose an atomic sulfur-bonded strategy to fabricate large-sized, crumpled, and antioxidative Ti_3C_2/Na_2S (TS) materials, which collaboratively promote compressed space and an antioxidant property. The groundbreaking strategy creates a precedent to devise Ti_3C_2 -based piezoresistive materials with comprehensive characteristics (i.e., large size, crumpled structure, and antioxidative properties) that pave the way for a highly sensitive and stable flexible piezoresistive sensor. This flexible piezoresistive sensor can be integrated into a wireless respiratory monitoring system, demonstrating significant potential for monitoring respiratory health.

SUMMARY

Flexible piezoresistive sensors have attracted great attention for the real-time monitoring of sleep apnea syndrome (SAS) through respiratory airflow. Although two-dimensional ultrathin Ti_3C_2 is regarded as a promising piezoresistive material, its poor structural compressibility and antioxidation limit its practical applications. Here, an innovative atomic sulfur-bonded strategy is proposed to fabricate large-sized, crumpled, and antioxidative Ti_3C_2/Na_2S (TS) flakes for preparing flexible piezoresistive sensors. The fundamental mechanism is rooted in the synergistic effect of lateral boundary assembly of Ti_3C_2 nanosheets into large flakes (~ 7 mm), lattice distortion to induce crumpled structures, and edge passivation by S^{2-} ions to mitigate oxidation (105 days). The crumpled microstructure provides abundant voids for enhanced compressibility and contact site variability, resulting in a 5-fold sensitivity improvement over the Ti_3C_2 sensor and an ultralow detection limit of 0.2 Pa. We demonstrate the practical application of highly sensitive and stable piezoresistive sensors integrated into a respiratory monitoring system for SAS detection.

INTRODUCTION

Sleep apnea syndrome (SAS) is a prevalent respiratory disorder characterized by recurrent partial or complete obstruction of the upper airway during sleep, which disrupts normal breathing pat-

terns and can impair the function of blood vessels supplying the heart and brain, potentially leading to life-threatening consequences.^{1,2} Nearly one billion individuals worldwide are estimated to be affected by this condition, and while polysomnography (PSG) is the gold standard for sleep monitoring, it is poorly

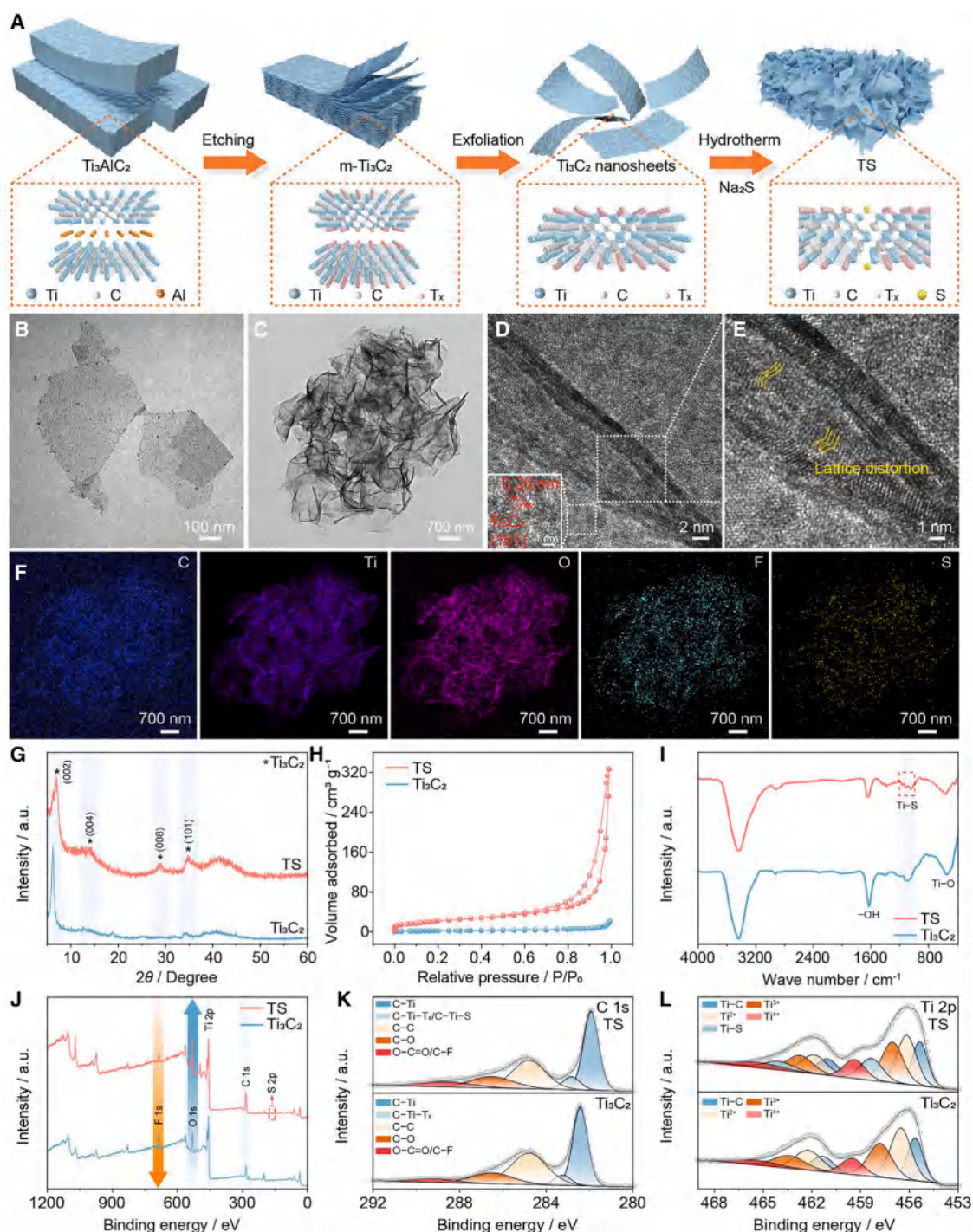


Figure 1. Characterization of Ti₃C₂ and TS material

(A) Synthesis diagram of TS sample.

(B and C) TEM images of Ti₃C₂ and TS.

(D) HRTEM image and enlarged lattice image of the surface region (inset).

(E) Local lattice distortion of crumpled region in (D).

(F) Elemental mapping images of TS.

(legend continued on next page)

wearable and inconvenient to operate.³ Flexible sensors can directly adhere to humans to achieve effective information transmission, which ensures perfect adaptation of sensing technology in terms of flexibility and comfort.⁴ Currently, the common monitoring signals used for SAS detection include pressure, temperature, and humidity, while temperature and humidity tend to accumulate relative to the environment over prolonged monitoring periods, which leads to inaccurate information.^{5,6} Flexible piezoresistive sensors track respiratory status by monitoring the slight pressure from respiratory airflow, which requires high sensitivity and stability to ensure accurate and reliable signals, primarily influenced by the piezoresistive materials.^{7,8} Therefore, it is urgent to devise a piezoresistive material that empowers a flexible piezoresistive sensor to integrate exceptional sensitivity with sustained stability for the precise monitoring of respiratory signals.

Two-dimensional (2D) Ti_3C_2 MXene has attracted extensive attention due to its large specific surface area, high conductivity, and adjustable surface terminal groups and is considered a promising material in the field of flexible piezoresistive sensors.^{9,10} However, its restricted interlayer spacing results in poor structural compressibility, causing it to inevitably suffer from deformation saturation, which hampers its feasibility as an independent piezoresistive material for the fabrication of high-performance pressure sensors.^{11,12} To date, combining Ti_3C_2 with polymers or elastic substrates is a common method to develop highly elastic piezoresistive materials, but it diminishes their subtle pressure detectability and sensitivity by compounding with these insulating materials.^{13–15} In principle, sensing performance primarily relies on alterations in electrical resistance influenced by the structure and electrical characteristics of piezoresistive materials, while material deformation is significantly determined by its geometry and mechanical properties.¹⁶ The effective method to improve sensing performance is to introduce microstructures into the sensing layer. More conductive pathways can be constructed in microstructures than in bulk structures, which results in amplified resistance change by enhancing the contact deformation ability.¹⁷ Up to now, most Ti_3C_2 -derived microstructures have been designed using the pre-stretching method, chemical treatment, and the template method, which increase experimental complexity, degrade inherent material properties, or require the assistance of elastic polymers for completion.^{18,19} However, there is still a significant gap to develop microstructures without the assistance of flexible materials.²⁰

Besides, the difficulty is that Ti_3C_2 tends to be oxidized and degrade rapidly over a few days in water and ambient conditions due to thermodynamically metastable surfaces, which triggers the deterioration of structural and sensing performances.^{21,22} In response, numerous strategies have been proposed to mitigate the oxidation of Ti_3C_2 by primarily preventing O_2 and/or H_2O from contacting Ti_3C_2 , which can be divided into three cat-

egories: altering storage conditions, applying antioxidants, and surface encapsulation.^{23–26} Nonetheless, the introduction of insulating additives will degrade the conductivity and chemical compatibility, and the weak interfacial interactions of Ti_3C_2 will restrict the application of the corresponding macrostructures. In addition, these methods are based on solution-mixing techniques, which are challenging to apply in devices. It is urgent to achieve a balance between antioxidation and applicability, which ensures a long shelf life without strict requirements for storage conditions. Therefore, how to collaboratively promote the sensitivity and stability of the sensor while exerting the excellent properties of Ti_3C_2 is the current research focus.

Herein, we innovatively propose an atomic sulfur-bonded strategy to design large-sized, crumpled, and antioxidative piezoresistive materials for flexible piezoresistive sensors to monitor SAS. The core mechanism lies in the synergistic effect of lateral boundary assembly of the Ti_3C_2 nanosheet to build large-sized sheets (~7 mm), the lattice distortion between Ti-S and Ti-C to induce crumpled structures, and edge passivation by anchoring S^{2-} ions to confer antioxidant stability (105 days). The crumpled microstructure effectively mitigates stress concentration and facilitates stress distribution, which provides more voids to expand compressive space and enhance the variability of contact sites. These properties improve the desirable sensing characteristics of the Ti_3C_2/Na_2S (TS) piezoresistive sensor (i.e., high sensitivity [7.8 kPa^{-1}], rapid responsiveness [~50 ms], stability [~10,000 cycles], and low detection threshold [~0.2 Pa]), which are particularly vital to monitor highly precise and tiny pressure signals. Assisted by operational amplifiers (Op-Amps) and the correlated double-sampling technique, the wireless respiratory monitoring system is dexterously integrated to monitor respiratory status. This strategy provides an effective approach to simultaneously resolve the deficiencies in the sensitivity and stability of Ti_3C_2 -based piezoresistive sensors.

RESULTS

Design and characterization of TS

The TS materials are synthesized by utilizing Na_2S and ultrathin Ti_3C_2 nanosheets as inducing agents and precursors, respectively, in hydrothermal conditions (Figures 1A and S1). The transmission electron microscopy (TEM) image shows that the initial Ti_3C_2 nanosheet has an ultrathin 2D plane structure with a lateral dimension of ~500 nm (Figure 1B). In comparison, the TS sample exhibits a large-sized, crumpled morphology with a predominant lateral size of ~7 mm (Figure 1C), indicating that the Ti_3C_2 nanosheets undergo secondary growth. High-resolution TEM (HRTEM) images reveal lattice fringes with a spacing of 0.26 nm across an extensive area in the TS sample, which matches the (101) interplanar spacing characteristic of Ti_3C_2 nanosheets (Figure 1D).²⁷ Moreover, lattice distortions are evident at the crumpled sites (Figure 1E). These distortions stem from

- (G) XRD patterns.
(H) N_2 adsorption and desorption isotherms.
(I) FT-IR spectra.
(J) XPS spectra.
(K and L) High-resolution spectra of C 1s and Ti 2p.

inhomogeneous localized structural deformations, which are induced by disparities in atomic sizes, bond lengths, and bond angles between Ti–S and Ti–C.^{28,29} Scanning TEM energy-dispersive X-ray mapping (STEM-EDX) shows the uniform element distribution of C, Ti, O, F, and S in TS (Figure 1F; Table S1). Moreover, the X-ray diffraction (XRD) pattern of TS exclusively exhibits characteristic peaks associated with Ti_3C_2 (Figure 1G), demonstrating that the incorporation of S ions preserves the crystalline structure of Ti_3C_2 . The observed lattice spacing for the (101) plane corroborates the findings from the HRTEM images. Notably, the broadening of characteristic peaks in TS is ascribed to the formation of crumpled microstructures. The N_2 adsorption-desorption isotherms of TS exhibit a distinctive type IV isotherm (Figure 1H). The Brunauer-Emmett-Teller (BET) method reveals that TS exhibits a specific surface area of $80.9 \text{ m}^2 \text{ g}^{-1}$, which is an order of magnitude greater than that of Ti_3C_2 ($6.9 \text{ m}^2 \text{ g}^{-1}$). This value surpasses previously reported specific surface areas of Ti_3C_2 (Table S2). Accordingly, the total pore volumes of TS and Ti_3C_2 are estimated to be 0.22 and $0.03 \text{ cm}^3 \text{ g}^{-1}$, respectively. The increases in specific surface area and pore volume can be attributed to the assembly and subsequent shrinkage of Ti_3C_2 nanosheets, which engenders a proliferation of contact sites. This structural evolution establishes the foundation for substantially improved sensitivity.³⁰ Compared with Ti_3C_2 nanosheets, the Fourier transform infrared (FT-IR) spectroscopy of TS reveals a new absorption peak at $1,048 \text{ cm}^{-1}$, which can be assigned to the Ti–S hanging bonds at the edge (Figure 1I).^{31,32} X-ray photoelectron spectroscopy (XPS) analysis of TS reveals a diminished peak intensity of –F groups and an enhanced peak intensity of –OH groups. It can be attributed to the susceptibility of –F groups to alkaline environments, which results in their substitution by –OH groups under alkaline conditions (Figure 1J).³³ A distinct peak at 282.84 eV emerges in the C 1s spectrum of TS, which is attributed to the formation of C–Ti–S bonds and overlaps the C–Ti–O bond region (Figure 1K).³⁴ The Ti 2p XPS spectrum of TS exhibits two new peaks at 458.3 and 464.0 eV , which can also be attributed to the Ti–S bond (Figure 1L).^{21,35} The emergence of S 2p signals in the XPS spectra of TS provides compelling evidence for the successful incorporation or modification of sulfur atoms into the structure. For S 2p in the spectrum of TS, the peaks corresponding to Ti–S (159.4 , 160.6 eV), C–Ti–S (164.5 , 165.7 eV), and S–O (167.3 , 168.5 eV) are observed, which result from the covalent bonds of nanosheet assembly, hanging bonds at the edge, and different oxidized sulfur forms of SO_x ($x = 2\text{--}4$) bonds (Figure S2).^{36,37} The S element constitutes approximately 0.32% of the atomic composition as determined by XPS, which corroborates well with the quantitative analysis obtained through STEM-EDX (Table S1). The cumulative evidence substantiates the successful fabrication of large-scale and crumpled TS structures, wherein S²⁻ ions serve as the key driving force for the directed assembly and growth of Ti_3C_2 nanosheets through edge adsorption and covalent bonding.

Evolution mechanism of TS

To comprehensively understand the evolution mechanism of TS materials, the intermediates of TS_x (where x represents reaction time, $x = 0.5$, 4 , 12 , and 24 h) at various assembly stages within 24 h are collected (Figures 2A–E). Initially, in the early stage of

the reaction, the individual Ti_3C_2 nanosheets gradually approach each other (Figure 2B). The crystalline structure integrity of $\text{TS}_{0.5}$ is well maintained, and the lateral dimensions increase to $\sim 1 \text{ mm}$ (Figures S3A and S4). This phenomenon is primarily attributed to the electronegative S²⁻ ions preferentially adsorbing onto the positively charged metastable Ti atoms at the edges of Ti_3C_2 nanosheets.³⁸ Simultaneously, these dangling S²⁻ ions are drawn toward the edges of neighboring Ti_3C_2 nanosheets due to electrostatic attractions between S²⁻ ions and metastable Ti atoms.³⁹ The conclusion is further confirmed by theoretical calculations based on density functional theory (DFT) (Note S1). The adsorption energy (E_{ad}) of S²⁻ on the edge of Ti_3C_2 is calculated as -8.10 eV , which is higher than its adsorption on the surface (-2.05 eV) (Figure 2F).

When the reaction proceeds for 4 h , the localized ordered splicing of individual nanosheets is completed via Ti–S–Ti bond bridging along their boundaries, resulting in larger structures accompanied by the emergence of crumpled morphologies (Figure 2C). The dominant lateral dimensions and specific surface area of TS_4 further increase to 2.5 mm and $62.6 \text{ m}^2 \text{ g}^{-1}$, respectively (Figure S3B). Theoretical calculations reveal that the Ti–S bond length ($\sim 2.4 \text{ \AA}$) exceeds that of the Ti–C bond ($\sim 2.1 \text{ \AA}$) (Figure 2G). This discrepancy in bond lengths between Ti–S and Ti–C induces lattice distortion for the formation of crumpled structures as the system seeks a stable configuration. As the reaction time prolongs to 12 h , TS_{12} exhibits dominant lateral dimensions to 4.5 mm and more pronounced crumpling for the specific surface area up to $64.1 \text{ m}^2 \text{ g}^{-1}$ (Figure S3C). XRD patterns show an obvious broadening of the diffraction peaks, corresponding to the intensification of the crumpling process. In addition to the lateral approach and assembly of independent nanosheets near the edges, the crumpled intermediates also exhibit lateral secondary assembly (Figures 2D and 2E). It can also be deduced that the specific surface area of TS_{12} is comparable to that of TS_4 ($62.6 \text{ m}^2 \text{ g}^{-1}$). As the reaction prolongs, the assembly edges of TS_{24} fully fuse to form a mature crumpled structure with a maximum lateral dimension of $\sim 7 \text{ mm}$ and a specific surface area of $80.9 \text{ m}^2 \text{ g}^{-1}$ (Figure S3D). Notably, the thickness at the edges of TS is comparable to that of the original nanosheets as evidenced by the contrast levels in TEM images, which indicates that TS growth occurs through lateral boundary assembly and lattice distortion, rather than multi-sheet flocculation, for large-sized, crumpled morphological evolution.

To further elucidate the influence of S²⁻ ions, the interactions of Ti_3C_2 nanosheets with different types of anions (i.e., Cl⁻, OH⁻, SO₄²⁻, and HS⁻) are investigated. Ti_3C_2 nanosheets undergo significant cleavage and oxidation to form TiO_2 in pure water and neutral solutions of NaCl or Na₂SO₄ (Figures 2H–2L, S5, and S6A–S6D). They undergo simultaneous alkalinization and oxidation to form crumpled Na₂Ti₃O₇ in NaOH aqueous solution (Figures 2J, 2L, and S6E).^{40–43} Even in the NaHS solution, Ti_3C_2 nanosheets are only oxidized to form TiO_2 nanoparticles (Figures 2K, 2L, and S6F). These results indicate that free S²⁻ ions and alkaline environments are equally crucial for the formation of large-sized, crumpled TS from Ti_3C_2 nanosheet assembly.³⁸ In essence, the formation of S–Ti–S bridging bonds between unsaturated Ti atoms on the edges of Ti_3C_2 and S²⁻ ions drives the assembly of Ti_3C_2 nanosheets, and the accompanied lattice distortion leads

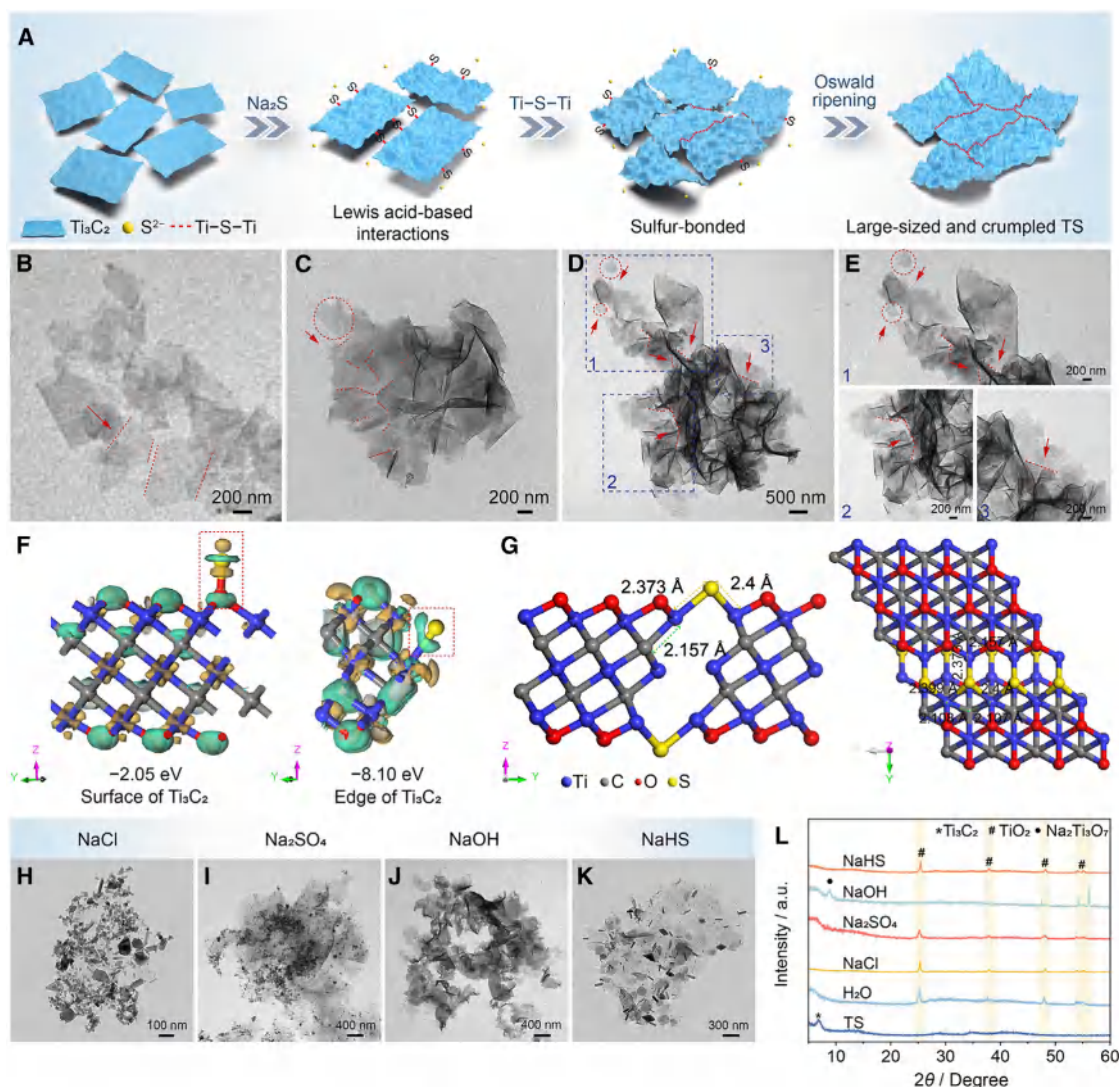


Figure 2. Evolution mechanism and structure characterization of TS materials

(A) Schematic illustration of the formation process for TS sample.

(B-D) TEM images of the formation process.

(E) Local enlarged image of (D).

(F) E_{ad} of S^{2-} adsorbed onto the surface of Ti_3C_2 and the edge of Ti_3C_2 .

(G) Side view and top view of TS optimized geometries.

(H-K) TEM images of different types of solution with Ti_3C_2 nanosheets under the hydrothermal reactions.

(L) XRD patterns.

to the stable crumpled configuration with reduced surface energy. Meanwhile, S^{2-} ions with strong reducibility anchoring on the edge sites will act as antioxidants for edge passivation.

Long-term stability of TS materials

To evaluate the antioxidant performance, the long-term stability of large-sized, crumpled TS materials is further investigated. The TS aqueous solution is stored in different atmospheres (i.e., air, Ar, O_2) (Figure S7). In an Ar atmosphere, TS dispersions undergo a complete transformation to an opaque, milky white appearance after 784 days. The time represents a 3-fold increase in oxidation

resistance compared to Ti_3C_2 (Figure S8). After air exposure for 21 days, the morphology of TS is well-preserved, and no characteristic peaks of TiO_2 are detected (Figures 3A and 3C). There are also no notable alterations in the characteristic $\text{Ti} 2\text{p}$ peaks at 455.85 and 461.75 eV of TS after 21 days (Figure 3D). Relative atomic percentages of 19.9%, 27.3%, 25.9%, 14.9%, and 12% correspond to Ti-C , Ti^{2+} , Ti^{3+} , Ti-S , and Ti^{4+} species, respectively, which exhibit negligible variations in the TS after 21 days (Figures 3E and S9; Table S3). In comparison, Ti_3C_2 endures obvious degradation from the edges accompanied by the formation of TiO_2 nanoparticles and pinholes (Figures 3B and 3C). A new

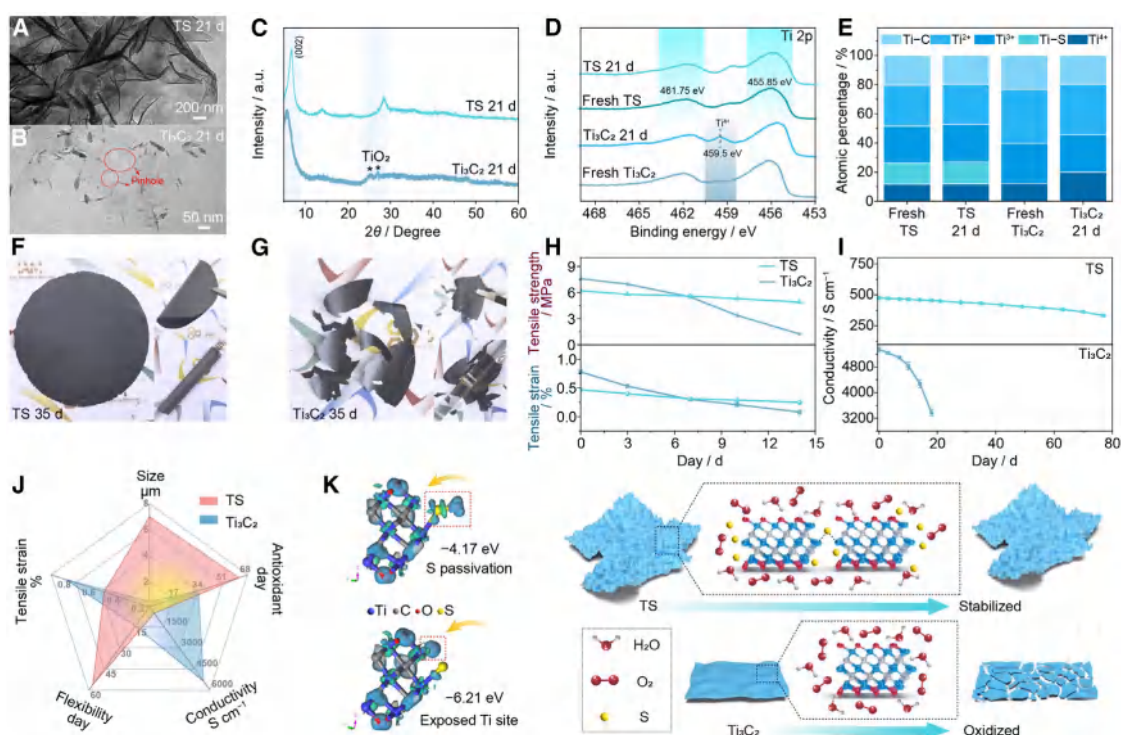


Figure 3. The performance characterization of Ti_3C_2 and TS

(A and B) TEM images of TS and Ti_3C_2 after being stored in the air for 21 days.

(C–E) XRD patterns (C), Ti 2p spectra (D), and XPS peak fitting results (E) of the Ti 2P regions of TS and Ti_3C_2 after 21 days.

(F and G) Photographs of TS and Ti_3C_2 after storage in air for 35 days.

(H and I) Tensile property retention (H) and conductivity (I) of TS and Ti_3C_2 with different times.

(J) Radar map of comprehensive properties of TS and Ti_3C_2 .

(K) Schematic illustration and the charge density difference of oxygen adsorbed.

peak at 459.5 eV appears, coinciding with an increased atomic fraction of Ti^{4+} from 12% to 20%, which indicates the formation of TiO_2 (Figures 3D and 3E).⁴⁴ The TS (002) peak completely vanishes and transforms into TiO_2 at 105 days, while Ti_3C_2 degrades entirely within a shorter period of 30 days (Figure S10). This reveals that TS obtains the enhanced antioxidant property in the solution phase, which surpasses the effectiveness of previously reported methods in the literature, including material modifications,^{25,45} optimization of storage conditions,⁴⁶ and the establishment of protective barriers at the surface or edges of Ti_3C_2 to impede water and oxygen interactions.^{21,22,47}

To investigate the electrical and mechanical stability in practical applications, the antioxidative performance of dried films is further investigated. Initially, TS films exhibit bending or curling deformations similar to those of Ti_3C_2 films (Figures S11 and S12). The cross-sectional SEM images show that the thickness of the TS film is ~6 nm, which is about twice as thick as that of the Ti_3C_2 film with an equivalent mass. The increased thickness is attributed to the crumpled microstructures with more voids and enlarged compressed space (Figure S13). The TS film exhibits a tensile fracture strength of 6.2 MPa and a tensile fracture strain of 0.47%, which are lower than those of the Ti_3C_2 film (7.59 MPa and 0.78%) (Figure S14). This disparity can be attributed to that large-sized TS nanosheets having a decreased surface cur-

vature, in which the stress and strain tend to concentrate at the crumpled regions, thereby hampering plastic deformation during bending and stretching states.⁴⁸ The TS film maintains complete integrity for up to 49 days and fully ruptures at 92 days, which is superior to the Ti_3C_2 film with a degradation time of only 14 days and a rupture time of 35 days (Figures 3F–3H). The electrical conductivity of the TS film is 475.24 S cm⁻¹ and can be well retained even in the cracked state at 77 days (Figures 3I and S15). However, the Ti_3C_2 film exhibits a severe rupture at 18 days and maintains only 63.2% of its initial conductivity. A comparative radar map illustrates the marked advantage of TS over Ti_3C_2 in terms of size and antioxidant properties (Figure 3J). The calculated E_{ad} of oxygen on the S^{2-} -passivated Ti sites is -4.17 eV, which is more positive than that on the Ti sites in Ti_3C_2 (-6.21 eV) (Figure 3K). This indicates a weaker coupling interaction between oxygen and S^{2-} -passivated edged sites, which effectively prevents edge-initiated oxidation of TS. In addition, stability is correlated with size, as smaller sheets are more susceptible to oxidation due to the abundant exposed active sites.⁴⁹ Consequently, increasing the sheet size through S bridging also emerges as a viable strategy to improve the antioxidant performance of Ti_3C_2 . In brief, it highlights the potential of the morphology and property regulation of Ti_3C_2 to enhance compressibility and mitigate oxidation through a novel atomic sulfur-bonded strategy.

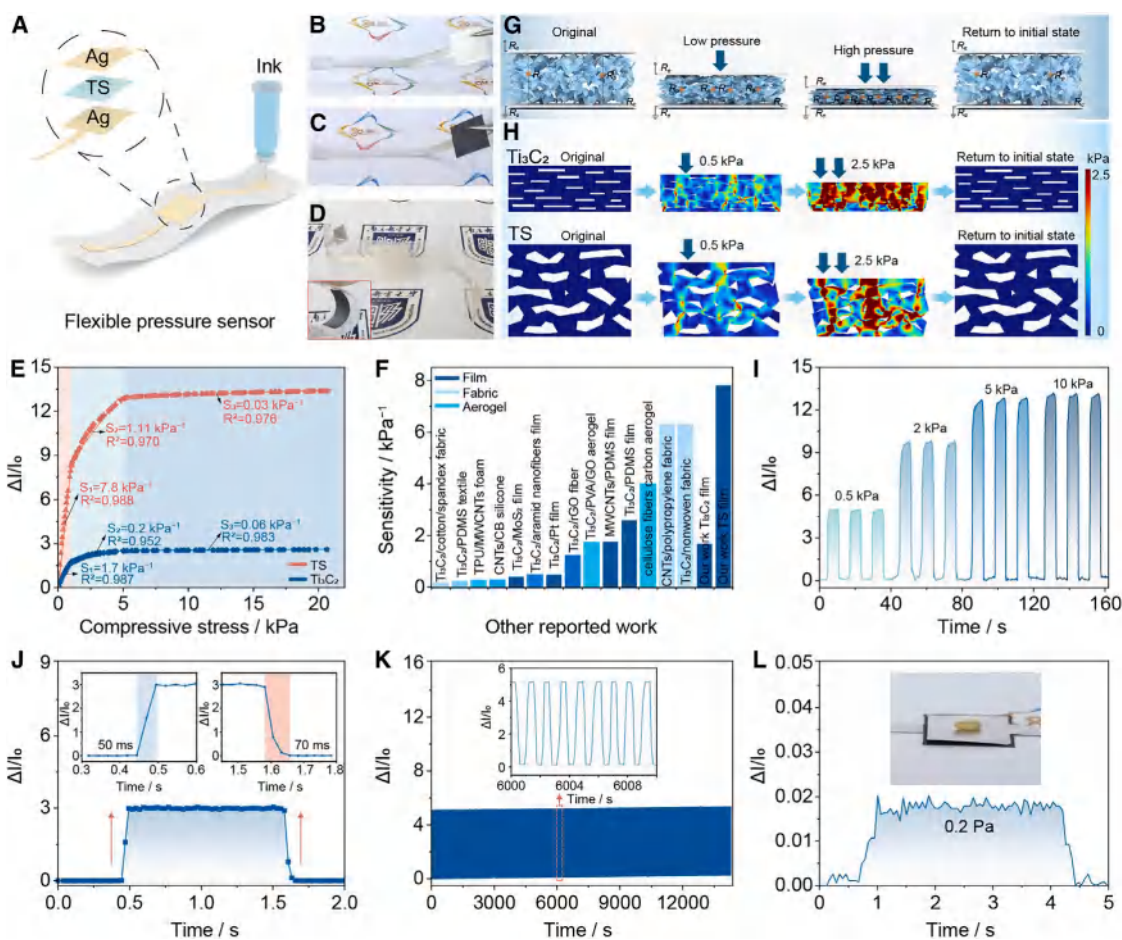


Figure 4. Demonstration of flexible piezoresistive sensor

- (A) Schematic illustration of TS flexible piezoresistive sensor.
- (B–D) The flexibility of Ag electrode, TS/Ag layers, and TS flexible piezoresistive sensor.
- (E) Sensitivity of the piezoresistive sensor with different sensing layers.
- (F) Sensitivity comparison for different piezoresistive sensors.
- (G) Sensing mechanism model of the TS piezoresistive sensor.
- (H) FEA simulation for the stress distribution.
- (I) Relative resistance changes under different pressures (i.e., 0.5, 2.0, 5.0, and 10.0 kPa).
- (J) Response time and recovery time at a pressure of 0.3 kPa.
- (K) Stability under 10,000 compression-release cycles at 0.5 kPa.
- (L) Response curve of the pressure provided by a sesame seed.

TS-based flexible piezoresistive sensor

The TS-based flexible piezoresistive sensor is constructed by a TS sensing layer and Ag electrode layers through the direct ink writing (DIW) technique (Figures 4A–D and S16–S18; Video S1). The TS piezoresistive sensor exhibits superior compression sensitivity compared to Ti_3C_2 across different pressure ranges (Figure 4E). In the low-pressure range (0–1.0 kPa), the sensitivity of the TS sensor is 7.8 kPa^{-1} , compared to 1.7 kPa^{-1} for the Ti_3C_2 sensor. In the medium pressure range (1.0–5.0 kPa), the TS sensor shows a sensitivity of 1.11 kPa^{-1} , while the Ti_3C_2 sensor reaches only 0.2 kPa^{-1} . Even in the high-pressure range (5.0–20.0 kPa), the TS sensor maintains a sensitivity of 0.03 kPa^{-1} , outperforming the 0.006 kPa^{-1} of the Ti_3C_2 sensor. The linearities of the TS

sensor for the three corresponding intervals are 0.988, 0.970, and 0.976, respectively. Notably, this exceptional performance is achieved without the incorporation of additional materials or reliance on an elastic matrix. The as-prepared TS sensors demonstrate superior sensitivity that surpasses the previously reported sensitivity of Ti_3C_2 -based sensors in the literature (Figure 4F). To elucidate the varying sensitivities across different pressure ranges, an equivalent circuit model is developed to represent the alterations in conductive pathways under varying applied pressures (Figure 4G). The initial resistance is defined as the electrode resistance (R_e), the internal resistance of the TS layer (R_p), and the contact resistance between TS and the electrode (R_c). Upon application of slight pressure, the protrusions of the

crumpled TS sensing layer establish closer contact with the Ag electrodes. This initiates the formation of denser conductive pathways for a changed R_p , which serves as the primary source of the overall resistance variation in the sensor. As pressure increases, the deformation of the TS layer leads to more densely compressed sheets, and the variable compression space progressively approaches saturation to decrease the sensitivity. Under extreme pressure, the TS sensing layer and Ag electrode layers achieve saturated contact, and the sensitivity plummets to its lowest point. The TS sensing layer quickly bounces back after releasing pressure, and the resistance returns to its initial state. Finite element analysis (FEA) simulation is further used to understand the compressive deformation behavior of TS (Figure 4H). Compared to the planar Ti_3C_2 , TS initially exhibits a crumpled and fluffy structure with more voids and increased compressive space. Under a pressure of 0.5 kPa, the TS effectively transmits the stress concentration from the initial contact point to neighboring ridges in the crumpled region, which consequently enhances the sensitivity. In contrast, the stress distribution within the Ti_3C_2 film propagates toward its interior. Upon reaching a pressure of 2.5 kPa, the contact area of Ti_3C_2 film essentially approaches saturation, whereas the TS layer still retains significant potential for further deformation. The sensing layer swiftly reverts to its original condition once pressure is released. The sensitivity retention rate of the sensor after aging 90 days is 94.23% with slight fluctuations (< 6%), confirming the excellent stability of the sensor (Figure S19). This observation underscores the efficacy that the incorporation of large-sized, crumpled microstructures can effectively enhance surface area variability, expand the compression range, and augment sensitivity.

Dynamic cyclic compression tests are conducted to explore the sensing performance of the TS piezoresistive sensor. Figure 4I depicts the relative current change during three consecutive pressure cycles at 0.5, 2.0, 5.0, and 10.0 kPa, respectively. Notably, the current response remains consistent under the same pressure, proving the consistency of the sensor and revealing a positive correlation between pressure and current variation. Under a certain pressure of 0.3 kPa, the response time and recovery time are 50 and 70 ms, respectively, which demonstrates the rapid response to external pressure stimuli (Figure 4J). After the pressure of 0.5 kPa is alternately loaded and unloaded onto the TS piezoresistive sensor over 10,000 cycles, the signal output without degradation demonstrates the remarkable stability and durability of the TS sensor (Figure 4K). Moreover, the SEM images reveal no obvious microscopic morphological or pore structure alterations within the same TS sensing layer before or after the compressive testing, which exhibits the excellent pore structure recoverability (Figure S20). The TS sensor demonstrates exceptional sensitivity by detecting a minute pressure of 0.2 Pa exerted by a single sesame seed (2 mg), as evidenced by instantaneous current fluctuations. This performance not only surpasses previously reported results but also underscores the capacity to discern extremely weak force signals (Figure 4L; Table S4). With its exceptional characteristics of high sensitivity, rapid response, stability, and low detection threshold, the TS piezoresistive sensor shows great potential as a reliable, real-time monitor for detecting both subtle and significant pressure variations.

Imperceptible and precise sign detection of TS flexible piezoresistive sensor

The ability of the sensor to detect subtle pressure signals directly impacts its high-precision performance.⁶⁴ The TS piezoresistive sensor demonstrates its exceptional sensitivity by accurately detecting minute pressures exerted by feathers, flower petals, and ladybugs, highlighting its remarkable capacity to discern subtle pressure fluctuations (Figure 5A). The carotid artery and radial artery have well-known subtle pulsations, which require the use of highly sensitive instruments for detection.⁶⁵ To validate the reliability of the sensor in humans, it is firmly affixed on the neck and wrist to capture the artery pulses in real time (Figures 5B and 5C). In addition, considering that the shape of the pulse waveform is closely related to some health conditions and SAS diseases, it is possible to derive and identify disease details by observing the pulse waveform. A continuous series of pulse-taking experiments are conducted, and the shapes of carotid pulses are similar and show response times of ~740 ms, indicating a heart rate of 81 beats min⁻¹. The enlarged single-pulse curve displays the typical pulse waveform of the percussion wave (P), tidal wave (T), and dicrotic wave (D), which is consistent with the results detected in other, related works.⁶⁶ The sensor attached to the radial artery also detects a steady and consistent pulse signal. The minimal baseline fluctuation demonstrates that the sensor effectively captures the changes in pulse waveforms and indicates a heart rate of 72 beats min⁻¹. In short, the sensor provides valuable information for monitoring pulse signals, which is important to demonstrate applications in intelligent healthcare. In addition to detecting tiny physiological signals, the sensor can be attached to the finger to generate response signals by tapping. By adopting the Morse code encryption mechanism, a new tapping communication system is constructed by matching the long and short pressing states of the finger to "dash" and "dot," respectively. Combined with the international Morse code table, specific information can be accurately transmitted (e.g., "HELP") by tapping fingers to realize the effective transmission of information (Figure S21). This innovation enables individuals with limited mobility to communicate effortlessly using Morse code, demonstrating significant potential in information transmission applications.

Wireless respiratory monitoring system of SAS by TS flexible piezoresistive sensor

SAS is a respiratory disorder that can induce bradypnea, weakness in breathing, and even transient cessation during sleep.⁶⁷ The utilization of data such as respiratory rate and depth for disease assessment represents a simple and effective approach. Generally, a complete respiratory cycle encompasses both inhalation and exhalation, which is often accompanied by weak pressure generated through the airflow. As the airflow exhaled from the nose touches the piezoresistive sensor, the airflow pressure is monitored through the changes in electrical signals, which can also identify different respiratory statuses. To verify the feasibility of respiratory monitoring, we preliminarily simulate four different breathing states, including normal breathing, apnea, rapid breathing, and deep breathing (Figure 5D). The respiratory rate and intensity show notable variations across different respiratory status. In normal breathing, the respiratory rate is 18 min⁻¹.

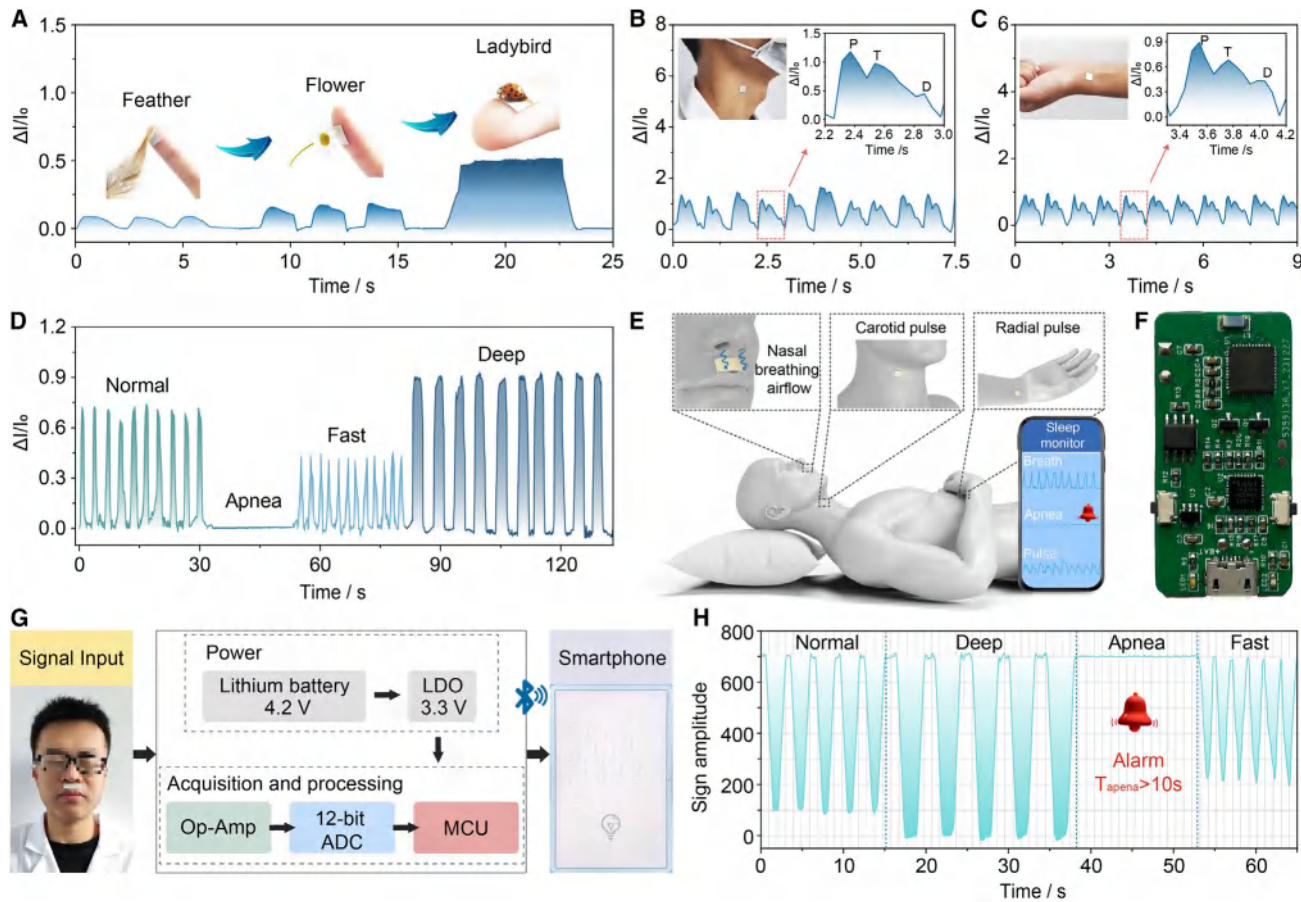


Figure 5. Application of TS flexible piezoresistive sensor

- (A) Response to the contact force of the feather, flower, and ladybird.
- (B–D) Response to the carotid artery, the radial artery, and different breathing states.
- (E) Schematic illustration of the sensor for monitoring physiological signals.
- (F) Wireless respiratory monitoring system module.
- (G) Block diagram of the wireless respiratory monitoring system.
- (H) Response of the wireless respiratory monitoring system to different respiratory statuses.

During the apnea state, there is no alteration in the pressure signal, and the electric current remains unchanged. In rapid breathing, the rate of respiration increases to 26 min^{-1} . In the process of deep breathing, there is a notable rise in breathing intensity owing to an increase in oxygen, while the rate of respiration decreases to 12 min^{-1} .

The wireless respiratory monitoring system is successfully developed by combining a TS piezoresistive sensor, a 12-bit high-precision analog-to-digital converter (ADC), a 32-bit microcontroller unit (MCU), a low-offset-voltage Op-Amp, a low-voltage demodulator (LDO), a 2.4 GHz ceramic antenna, and Bluetooth (Figures 5E, 5F, and S22). The LDO regulator converts the 4.2 V output voltage of lithium batteries to 3.3 V, providing power to the MCU and Op-Amp. The Op-Amp further amplifies the tiny respiratory signals detected by sensors to ensure the accuracy of the data. The monitoring signal is converted and processed by the ADC and MCU processor and wirelessly transmitted to the smartphone terminal via the Bluetooth module (Figure 5G). After considering the signal variations of the sensor

under different breathing depths and velocities, a real-time calibration technique is developed to accurately monitor fluctuations in breathing signals. By combining the correlated double-sampling technique with the ADC hardware circuit module, sampling accuracy can be improved, and the impact of noise on the signal can be reduced. The breathing status of the tester can be monitored in real time with a mobile phone, and alerts can be triggered when the breathing signal is paused above 10 s or the breathing rate rises to 27 min^{-1} , indicating a breathing abnormality.⁶⁸ The experiment assesses the respiratory condition for SAS diagnosis. The four breathing states can be accurately detected, which exhibits steady and repeatable electrical signs, efficiently tracking the breathing abnormality to promptly trigger the alarm (Figure 5H; Video S2). The results suggest that the wireless respiratory monitoring system demonstrates great responsiveness and discernibility under different breath modes, which indicates its outstanding potential to diagnose SAS. Compared to existing sleep health monitoring systems, the standout advantages of this system lie in its wireless

transmission capability and portability, which address the issue of patients being tethered to traditional monitoring equipment, thereby enhancing patient comfort. Additionally, its high-precision monitor and real-time data analysis technology can diagnose SAS more accurately, which provides patients with timely health alerts and effective treatment recommendations.

DISCUSSION

In summary, we first developed large-sized, crumpled, and anti-oxidative TS flakes through a novel atomic sulfur-bonded Ti_3C_2 nanosheet strategy to construct a highly sensitive and stable piezoresistive sensor to monitor SAS. The formation mechanism of TS is involved in the synergistic effect of lateral boundary assembly of individual Ti_3C_2 units (~ 500 nm) for large-sized nanosheets (~ 7 mm), lattice distortion induced by the differentiation of Ti-S and Ti-C for crumpled structures ($80.9 \text{ m}^2 \text{ g}^{-1}$), and edge passivation by anchoring S^{2-} ions for antioxidant stability (105 days). The TS piezoresistive sensor exhibits the exceptional comprehensive characteristics of high sensitivity (7.8 kPa^{-1}), rapid response (~ 50 ms), stability ($\sim 10,000$ cycles), and low detection threshold ($\sim 0.2 \text{ Pa}$) due to the crumpled microstructure providing more voids to expand the compressive space and facilitating stress transfer to enhance contact site variability. As a result, a wireless respiratory monitoring system of SAS based on a TS flexible piezoresistive sensor enables the accurate identification of different respiratory states, including normal breathing, apnea, rapid breathing, and deep breathing, offering real-time feedback for abnormal sleep breathing. This work paves the way to fabricating highly sensitive and greatly compressible piezoresistive sensors for portable and wearable applications in SAS monitoring.

EXPERIMENTAL PROCEDURES

Materials

Ti_3AlC_2 powder was purchased from Jilin 11 Technology (Jilin, China). Lithium fluoride (LiF), sodium hydrosulfide (NaHS), and dimethyl sulfoxide (DMSO) were purchased from Aladdin Biochemical Technology. Hydrochloric acid (HCl) solution and sodium sulfide (Na_2S) were obtained from Shanghai Sino-pharm Group. Sodium sulfate (Na_2SO_4) and sodium chloride (NaCl) were purchased from Sinopharm Chemical Reagent. Sodium hydroxide (NaOH) was purchased from Xilong Scientific. All materials in this work were used as received without further purification.

Characterization

SEM images were observed by a field emission scanning electron microscope (Hitachi S-4800). TEM imaging was performed by a transmission electron microscope (Hitachi HT7700). HRTEM imaging was carried out by a high-resolution transmission electron microscope at an acceleration voltage of 200 kV (FEI Talos F200X). XRD patterns were recorded by an X-ray diffractometer (Bruker AXS D8 Advance) using Cu K_{α} radiation ($\lambda = 1.5406 \text{ \AA}$) over the range of $2\theta = 5.0^\circ$ – 60.0° . FTIR spectroscopy was obtained using a Fourier transform infrared spectrophotometer (PerkinElmer Spectrum Two). XPS was performed by a X-ray photoelectron spectrometer (Thermo ESCALAB 250Xi). N_2 isotherms were measured on a surface area and pore size analyzer (Micromeritics ASAP2020 (M+C)). Thin-film sheet resistance was measured by a dual electric digital four-probe tester (Jingge ST2263). Tensile property was performed by a tensile testing tester (Instron 3365) with a loading rate of 0.1 mm min^{-1} . The stress (s) and strain (ϵ) were represented as $s = F/S$ and $\epsilon = (l - l_0)/l_0$ $\times 100\%$, where F was the load (N), S was the cross-section area (m^2), l_0 was the initial length (mm), and l was the broken length (mm). Electrodes and sensing layers were printed by a microelectronics printer (Prtronic Scientific

3A). The electrical signal of the flexible piezoresistive sensor was obtained by a semiconductor parameter analyzer (Keithley 4200A-SCS) at a voltage of 1 V. The sensor was placed in the tension and compression tester (Mark-10 ESM303) with a compression rate of 0.5 mm min^{-1} .

Synthesis of ultrathin Ti_3C_2 nanosheets

The multilayer Ti_3C_2 (m- Ti_3C_2) bulks were first fabricated via etching the Al layer from Ti_3AlC_2 bulks. First, LiF (1 g) was dissolved in HCl (9 M, 20 mL). Then, the Ti_3AlC_2 bulks (1 g) were added to the mixture and incubated at 60°C for 24 h. Subsequently, the products were washed with deionized water until the pH was above 6. Afterward, the samples were dried under a vacuum for 12 h to obtain the m- Ti_3C_2 . Next, m- Ti_3C_2 was dissolved in deionized water and sonicated for 1 h. Finally, the dispersion was centrifuged at 3,500 rpm for 1 h. The ultrathin Ti_3C_2 nanosheets were collected.

Synthesis of TS materials

First, 6 mmol Na_2S was dissolved in 9.86 mL of deoxygenated water. Then, 2.14 mL of Ti_3C_2 nanosheet dispersion was added to the Na_2S aqueous and retained at 180°C for 24 h. Afterward, the products were washed with deoxygenated water until the pH was neutral, and the precipitation was collected for further application.

Synthesis of individual Ti_3C_2 or TS film

The film was fabricated through a vacuum-assisted filtering method. The mixed cellulose ester membrane was employed to filter the Ti_3C_2 nanosheet dispersion or TS solution. The resultant film was dried at room temperature.

Synthesis of TS inks

First, TS dispersion was centrifuged at 10,000 rpm for 10 min. Then, the precipitation was dispersed in DMSO uniformly by ultrasonication. Finally, the dispersion was centrifuged at 2,000 rpm for 5 min.

Synthesis of flexible piezoresistive sensor

The conductive silver paste was first used to print the silver electrode on the flexible substrate. TS inks were then printed on the silver electrode as the sensing layer. The piezoresistive sensor was constructed with an Ag electrode and TS/Ag as a sensing layer and electrode layer, respectively, by attaching them face to face.

Sensing test of flexible piezoresistive sensor

The sensor is placed on the compression tester and connected to the semiconductor parameter analyzer through copper foil. The sensing sensitivity was expressed as follows:

$$S = \frac{DI/I_0}{P} = \frac{DR/R_0}{P} \quad (\text{Equation 1})$$

where P is the pressure, DI and I_0 denote the relative current change and initial current, respectively, and DR and R_0 denote the relative resistance change and initial resistance, respectively. Similarly, the changes in resistance can serve as an indicator of alterations in sensitivity. The real-time resistance (R) of the equivalent circuit can be expressed as follows:

$$R = R_e + R_c + R_p; \quad (\text{Equation 2})$$

where R_e is the resistance of electrodes, R_c is the contact resistance between TS and electrodes, and R_p is defined as the resistance of the TS sensing layer during the compression. The resistance can further be expressed as

$$R = \frac{\rho \cdot 3T}{A}; \quad (\text{Equation 3})$$

where ρ represents the resistivity of the conducting material, T represents the thickness, and A represents the cross-sectional area. The R calculation formula can be rewritten as

$$R = \frac{r_e 3 T_e}{A_e} + \frac{r_c 3 T_c}{A_c} + \frac{r_p 3 T_p}{A_p} \quad (\text{Equation 4})$$

Integration of wireless respiratory monitoring system

The integrated printing circuit board (PCB) was connected by a double layer of lithographic copper conductors over FR-4 plates, with an overall PCB size of 43.65 × 21.24 mm². The hardware circuit integrated a low-voltage drop regulator (LDO, LP2992AIM5X-3.3/NOPB, TI), a low-offset Op-Amp (OP07CDR, TI), a 32-bit MCU(ESP32-PICO-D4, ESPRESSIF) with 12-bit high-precision ADC function and Bluetooth low energy, a 2.4 GHz ceramic antenna (RFECA3216060A1T, Walsin), a USB to the serial chip (CP2102-GMR, SILICON LABS), and passive components such as resistors, capacitors, and inductors. The TS flexible piezoresistive sensor was connected to the monitoring system through wires. The monitoring signal was further sent to the smartphone via Bluetooth.

RESOURCE AVAILABILITY

Lead contact

Further information and requests for resources and reagents should be directed to and will be fulfilled by the lead contact, Weiwei Zhao (iamwwzhao@njupt.edu.cn).

Materials availability

This study did not generate new unique reagents.

Data and code availability

All data and code generated during the study are available from the [lead contact](#) upon reasonable request.

ACKNOWLEDGMENTS

This work was supported by the National Natural Science Foundation of China (62174086, 62288102, and 62404113), the Outstanding Youth Foundation of Jiangsu Province (BK20240139), the Qinglan Project of Jiangsu Province of China, and the Postgraduate Research and Practice Innovation Program of Jiangsu Province (KYCX23_0985).

AUTHOR CONTRIBUTIONS

W.Z., W.H., and Q.Z. conceived the idea for this work and supervised the project. Y.B. contributed to the synthesis work, measurements, and application study. L.W. performed theoretical calculations and analysis. X.Z., N.D., Y.F., Z.Y., W.W., and F.L. carried out the device fabrication and characterization. Y.C., Y.Z., J.L., F.G., and S.L. performed sensing characterization experiments. All authors contributed to analyzing the data.

DECLARATION OF INTERESTS

The authors declare no competing interests.

SUPPLEMENTAL INFORMATION

Supplemental information can be found online at <https://doi.org/10.1016/j.matt.2024.11.021>.

Received: August 27, 2024

Revised: October 28, 2024

Accepted: November 18, 2024

Published: December 16, 2024

REFERENCES

1. Supperpool, A., Lyons, D.G., Broom, E., and Rihel, J. (2024). Sleep pressure modulates single-neuron synapse number in zebrafish. *Nature* 629, 639–645. <https://doi.org/10.1038/s41586-024-07367-3>.
2. Slutsky, I. (2024). Linking activity dyshomeostasis and sleep disturbances in alzheimer disease. *Nat. Rev. Neurosci.* 25, 272–284. <https://doi.org/10.1038/s41583-024-00797-y>.
3. Lv, R., Liu, X., Zhang, Y., Dong, N., Wang, X., He, Y., Yue, H., and Yin, Q. (2023). Pathophysiological mechanisms and therapeutic approaches in obstructive sleep apnea syndrome. *Signal Transduct. Targeted Ther.* 8, 218. <https://doi.org/10.1038/s41392-023-01496-3>.
4. Lee, J.H., Cho, K., and Kim, J.K. (2024). Age of flexible electronics: emerging trends in soft multifunctional sensors. *Adv. Mater.* 36, 2310505. <https://doi.org/10.1002/adma.202310505>.
5. Sun, J., Xiu, K., Wang, Z., Hu, N., Zhao, L., Zhu, H., Kong, F., Xiao, J., Cheng, L., and Bi, X. (2023). Multifunctional wearable humidity and pressure sensors based on biocompatible graphene/bacterial cellulose bio-aerogel for wireless monitoring and early warning of sleep apnea syndrome. *Nano Energy* 108, 108215. <https://doi.org/10.1016/j.nanoen.2023.108215>.
6. Liu, H., Sun, K., Guo, X.L., Liu, Z.L., Wang, Y.H., Yang, Y., Yu, D., Li, Y.T., and Ren, T.L. (2022). An ultrahigh linear sensitive temperature sensor based on PANI: graphene and PDMS hybrid with negative temperature compensation. *ACS Nano* 16, 21527–21535. <https://doi.org/10.1021/acsnano.2c10342>.
7. Luo, Y., Abidian, M.R., Ahn, J.H., Akinwande, D., Andrews, A.M., Antonietti, M., Bao, Z., Berggren, M., Berkey, C.A., Bettinger, C.J., et al. (2023). Technology roadmap for flexible sensors. *ACS Nano* 17, 5211–5295. <https://doi.org/10.1021/acsnano.2c12606>.
8. Hu, L., Chee, P.L., Sugiantoro, S., Yu, Y., Shi, C., Yan, R., Yao, Z., Shi, X., Zhi, J., Kai, D., et al. (2023). Hydrogel-based flexible electronics. *Adv. Mater.* 35, 2205326. <https://doi.org/10.1002/adma.202205326>.
9. Li, W., Zhou, T., Zhang, Z., Li, L., Lian, W., Wang, Y., Lu, J., Yan, J., Wang, H., Wei, L., and Cheng, Q. (2024). Ultrastrong MXene film induced by sequential bridging with liquid metal. *Science* 385, 62–68. <https://doi.org/10.1126/science.ad04257>.
10. Ma, Y., Liu, N., Li, L., Hu, X., Zou, Z., Wang, J., Luo, S., and Gao, Y. (2017). A highly flexible and sensitive piezoresistive sensor based on MXene with greatly changed interlayer distances. *Nat. Commun.* 8, 1207. <https://doi.org/10.1038/s41467-017-01136-9>.
11. Qin, R., Nong, J., Wang, K., Liu, Y., Zhou, S., Hu, M., Zhao, H., and Shan, G. (2024). Recent advances in flexible pressure sensors based on MXene materials. *Adv. Mater.* 36, 2312761. <https://doi.org/10.1002/adma.202312761>.
12. Wu, Z., Wei, L., Tang, S., Xiong, Y., Qin, X., Luo, J., Fang, J., and Wang, X. (2021). Recent progress in Ti₃C₂T_x MXene-based flexible pressure sensors. *ACS Nano* 15, 18880–18894. <https://doi.org/10.1021/acsnano.1c08239>.
13. Wang, Y., Guo, T., Tian, Z., Shi, L., Barman, S.C., and Alshareef, H.N. (2023). MXenes for soft robotics. *Matter* 6, 2807–2833. <https://doi.org/10.1016/j.matt.2023.07.013>.
14. Lai, O.T., Zhao, X.H., Sun, Q.J., Tang, Z., Tang, X.G., and Roy, V.A.L. (2023). Emerging MXene-based flexible tactile sensors for health monitoring and haptic perception. *Small* 19, 2300283. <https://doi.org/10.1002/smll.202300283>.
15. Yin, T., Cheng, Y., Hou, Y., Sun, L., Ma, Y., Su, J., Zhang, Z., Liu, N., Li, L., and Gao, Y. (2022). 3D porous structure in MXene/PANI foam for a high-performance flexible pressure sensor. *Small* 18, 2204806. <https://doi.org/10.1002/smll.202204806>.
16. Xu, C., Chen, J., Zhu, Z., Liu, M., Lan, R., Chen, X., Tang, W., Zhang, Y., and Li, H. (2024). Flexible pressure sensors in human-machine interface applications. *Small* 20, 2306655. <https://doi.org/10.1002/smll.202306655>.
17. Shi, Z., Meng, L., Shi, X., Li, H., Zhang, J., Sun, Q., Liu, X., Chen, J., and Liu, S. (2022). Morphological engineering of sensing materials for flexible pressure sensors and artificial intelligence applications. *Nano-Micro Lett.* 14, 141. <https://doi.org/10.1007/s40820-022-00874-w>.

18. Lei, D., Liu, N., Su, T., Zhang, Q., Wang, L., Ren, Z., and Gao, Y. (2022). Roles of MXene in pressure sensing: preparation, composite structure design, and mechanism. *Adv. Mater.* 34, 2110608. <https://doi.org/10.1002/adma.202110608>.
19. Pitcheri, R., Chittibabu, S.K., Sangaraju, S., Jarsangi, B., Al-Asbahi, B.A., Minnam Reddy, V.R., and Kim, W.K. (2024). Emerging trends of 3D architec-tonic MXene-based flexible pressure sensors as multimodal medical devices. *Coord. Chem. Rev.* 499, 215527. <https://doi.org/10.1016/j.ccr.2023.215527>.
20. Shi, X., Fan, X., Zhu, Y., Liu, Y., Wu, P., Jiang, R., Wu, B., Wu, H.A., Zheng, H., Wang, J., et al. (2022). Pushing detectability and sensitivity for subtle force to new limits with shrinkable nanochannel structured aerogel. *Nat. Commun.* 13, 1119. <https://doi.org/10.1038/s41467-022-28760-4>.
21. Zhao, X., Vashisth, A., Prehn, E., Sun, W., Shah, S.A., Habib, T., Chen, Y., Tan, Z., Lutkenhaus, J.L., Radovic, M., and Green, M.J. (2019). Antioxidants unlock shelf-stable $Ti_3C_2T_x$ (MXene) nanosheet dispersions. *Matter* 1, 513–526. <https://doi.org/10.1016/j.matt.2019.05.020>.
22. Natu, V., Hart, J.L., Sokol, M., Chiang, H., Taheri, M.L., and Barsoum, M.W. (2019). Edge capping of 2D-MXene sheets with polyanionic salts to mitigate oxidation in aqueous colloidal suspensions. *Angew. Chem. Int. Ed. Engl.* 58, 12655–12660. <https://doi.org/10.1002/anie.201906138>.
23. Zhang, Q., Lai, H., Fan, R., Ji, P., Fu, X., and Li, H. (2021). High concentration of $Ti_3C_2T_x$ MXene in organic solvent. *ACS Nano* 15, 5249–5262. <https://doi.org/10.1021/acsnano.0c10671>.
24. Liu, N., Li, Q., Wan, H., Chang, L., Wang, H., Fang, J., Ding, T., Wen, Q., Zhou, L., and Xiao, X. (2022). High-temperature stability in air of $Ti_3C_2T_x$ MXene-based composite with extracted bentonite. *Nat. Commun.* 13, 5551. <https://doi.org/10.1038/s41467-022-33280-2>.
25. Choi, J., Oh, M.S., Cho, A., Ryu, J., Kim, Y.J., Kang, H., Cho, S.Y., Im, S.G., Kim, S.J., and Jung, H.T. (2023). Simple approach to enhance long-term environmental stability of MXene using initiated chemical vapor deposition surface coating. *ACS Nano* 17, 10898–10905. <https://doi.org/10.1021/acsnano.3c02668>.
26. Ma, Y., Yue, Y., Zhang, H., Cheng, F., Zhao, W., Rao, J., Luo, S., Wang, J., Jiang, X., Liu, Z., et al. (2018). 3D synergistical MXene/reduced graphene oxide aerogel for a piezoresistive sensor. *ACS Nano* 12, 3209–3216. <https://doi.org/10.1021/acsnano.7b06909>.
27. Zhao, W., Jin, B., Wang, L., Ding, C., Jiang, M., Chen, T., Bi, S., Liu, S., and Zhao, Q. (2022). Ultrathin Ti_3C_2 nanowires derived from multi-layered bulks for high-performance hydrogen evolution reaction. *Chin. Chem. Lett.* 33, 557–561. <https://doi.org/10.1016/j.ccl.2021.07.035>.
28. Gupta, N., Sahu, R.K., Mishra, T., and Bhattacharya, P. (2022). Micro-wave-assisted rapid synthesis of titanium phosphate free phosphorus doped Ti_3C_2 MXene with boosted pseudocapacitance. *J. Mater. Chem. A* 10, 15794–15810. <https://doi.org/10.1039/D2TA04061A>.
29. Shah, S.A., Habib, T., Gao, H., Gao, P., Sun, W., Green, M.J., and Radovic, M. (2016). Template-free 3D titanium carbide ($Ti_3C_2T_x$) MXene particles crumpled by capillary forces. *Chem. Commun.* 53, 400–403. <https://doi.org/10.1039/C6CC07733A>.
30. Shen, Q., Song, Q., Mai, Z., Lee, K.R., Yoshioka, T., Guan, K., Gonzales, R.R., and Matsuyama, H. (2023). When self-assembly meets interfacial polymerization. *Sci. Adv.* 9, eadf6122. <https://doi.org/10.1126/sciadv.adf6122>.
31. Zhang, G., Zhang, Y.C., Nadagouda, M., Han, C., O'Shea, K., El Sheikh, S.M., Ismail, A.A., and Dionysiou, D.D. (2014). Visible light-sensitized S, N and Co co-doped polymorphic TiO_2 for photocatalytic destruction of microcystin-LR. *Appl. Catal. B Environ.* 144, 614–621. <https://doi.org/10.1016/j.apcatb.2013.07.058>.
32. Han, C., Pelaez, M., Likodimos, V., Kontos, A.G., Falaras, P., O'Shea, K., and Dionysiou, D.D. (2011). Innovative visible light-activated sulfur doped TiO_2 films for water treatment. *Appl. Catal., B: Environ. Energy* 107, 77–87. <https://doi.org/10.1016/j.apcatb.2011.06.039>.
33. Du, Y., Yan, Z., You, W., Men, Q., Chen, G., Lv, X., Wu, Y., Luo, K., Zhao, B., Zhang, J., and Che, R. (2023). Balancing MXene surface termination and interlayer spacing enables superior microwave absorption. *Adv. Funct. Mater.* 33, 2301449. <https://doi.org/10.1002/adfm.202301449>.
34. Yang, X., Yao, Y., Wang, Q., Zhu, K., Ye, K., Wang, G., Cao, D., and Yan, J. (2022). 3D macroporous oxidation-resistant $Ti_3C_2T_x$ MXene hybrid hydrogels for enhanced supercapacitive performances with ultralong cycle life. *Adv. Funct. Mater.* 32, 2109479. <https://doi.org/10.1002/adfm.202109479>.
35. Bao, W., Shuck, C.E., Zhang, W., Guo, X., Gogotsi, Y., and Wang, G. (2019). Boosting performance of Na-S batteries using sulfur-doped $Ti_3C_2T_x$ MXene nanosheets with a strong affinity to sodium polysulfides. *ACS Nano* 13, 11500–11509. <https://doi.org/10.1021/acsnano.9b04977>.
36. Luo, J., Zheng, J., Nai, J., Jin, C., Yuan, H., Sheng, O., Liu, Y., Fang, R., Zhang, W., Huang, H., et al. (2019). Atomic sulfur covalently engineered interlayers of Ti_3C_2 MXene for ultra-fast sodium-ion storage by enhanced pseudocapacitance. *Adv. Funct. Mater.* 29, 1808107. <https://doi.org/10.1002/adfm.201808107>.
37. Huo, X., Wang, X., Li, Z., Liu, J., and Li, J. (2020). Two-dimensional composite of $D-Ti_3C_2T_x@S@TiO_2$ (MXene) as the cathode material for aluminum-ion batteries. *Nanoscale* 12, 3387–3399. <https://doi.org/10.1039/C9NR09944A>.
38. Natu, V., Sokol, M., Verger, L., and Barsoum, M.W. (2018). Effect of edge charges on stability and aggregation of $Ti_3C_2T_x$ MXene colloidal suspensions. *J. Phys. Chem. C* 122, 27745–27753. <https://doi.org/10.1021/acs.jpcc.8b08860>.
39. Liang, X., Rangom, Y., Kwok, C.Y., Pang, Q., and Nazar, L.F. (2017). Interwoven MXene nanosheet/carbon-nanotube composites as Li-S cathode hosts. *Adv. Mater.* 29, 1603040. <https://doi.org/10.1002/adma.201603040>.
40. Li, Y., Deng, X., Tian, J., Liang, Z., and Cui, H. (2018). Ti_3C_2 MXene-derived Ti_3C_2/TiO_2 nanoflowers for noble-metal-free photocatalytic overall water splitting. *Appl. Mater. Today* 13, 217–227. <https://doi.org/10.1016/j.apmt.2018.09.004>.
41. Dong, Y., Wu, Z.S., Zheng, S., Wang, X., Qin, J., Wang, S., Shi, X., and Bao, X. (2017). Ti_3C_2 MXene-derived sodium/potassium titanate nanoribbons for high-performance sodium/potassium ion batteries with enhanced capacities. *ACS Nano* 11, 4792–4800. <https://doi.org/10.1021/acsnano.7b01165>.
42. Yao, Y., Ma, Y., Chen, C., Zhu, K., Wang, G., Cao, D., and Yan, J. (2024). Enhanced sodium-storage performances of crumpled MXene nanosheets via alkali treatment-induced active ammonium ions. *J. Colloid Interface Sci.* 670, 647–657. <https://doi.org/10.1016/j.jcis.2024.05.124>.
43. Zhang, J., Zhang, X., Sun, W., Zhou, W., and Yue, W. (2024). Chemical scissor-enabled synthesis of $Ti_3C_2T_x$ MXene nanowires for selective oxygen reduction to hydrogen peroxide. *Appl. Surf. Sci.* 648, 159068. <https://doi.org/10.1016/j.apsusc.2023.159068>.
44. Peng, M., Wang, L., Li, L., Tang, X., Huang, B., Hu, T., Yuan, K., and Chen, Y. (2022). Manipulating the interlayer spacing of 3D MXenes with improved stability and zinc-ion storage capability. *Adv. Funct. Mater.* 32, 2109524. <https://doi.org/10.1002/adfm.202109524>.
45. Ji, J., Zhao, L., Shen, Y., Liu, S., and Zhang, Y. (2019). Covalent stabilization and functionalization of MXene via silylation reactions with improved surface properties. *FlatChem* 17, 100128. <https://doi.org/10.1016/j.flatc.2019.100128>.
46. Zhao, X., Vashisth, A., Blivin, J.W., Tan, Z., Holta, D.E., Kotasthane, V., Shah, S.A., Habib, T., Liu, S., Lutkenhaus, J.L., et al. (2020). pH, nanosheet concentration, and antioxidant affect the oxidation of $Ti_3C_2T_x$ and Ti_2CT_x MXene dispersions. *Adv. Mater. Interfac.* 7, 2000845. <https://doi.org/10.1002/admi.2020000845>.
47. Wang, X.Y., Liao, S.Y., Huang, H.P., Wang, Q.F., Shi, Y.Y., Zhu, P.L., Hu, Y.G., Sun, R., and Wan, Y.J. (2023). Enhancing the chemical stability of MXene through synergy of hydrogen bond and coordination bond in

- aqueous solution. *Small Methods* 7, 2201694. <https://doi.org/10.1002/smtd.202201694>.
48. Wang, Y., Zhao, Y., Han, Y., Li, X., Dai, C., Zhang, X., Jin, X., Shao, C., Lu, B., Wang, C., et al. (2022). Fixture-free omnidirectional prestretching fabrication and integration of crumpled in-plane micro-supercapacitors. *Sci. Adv.* 8, eabn8338. <https://doi.org/10.1126/sciadv.abn8338>.
49. Zhang, C.J., Pinilla, S., McEvoy, N., Cullen, C.P., Anasori, B., Long, E., Park, S.H., Seral Ascaso, A., Shmeliiov, A., Krishnan, D., et al. (2017). Oxidation stability of colloidal two-dimensional titanium carbides (MXenes). *Chem. Mater.* 29, 4848–4856. <https://doi.org/10.1021/acs.chemmater.7b00745>.
50. Chang, K., Meng, J., Guo, M., Li, L., Liu, T., and Huang, Y. (2023). Flexible and breathable MXene fabrics for highly sensitive human motion monitoring. *Chem. Eng. J.* 474, 145532. <https://doi.org/10.1016/j.cej.2023.145532>.
51. Yao, D., Tang, Z., Liang, Z., Zhang, L., Sun, Q.J., Fan, J., Zhong, G., Liu, Q.X., Jiang, Y.P., Tang, X.G., et al. (2023). Adhesive, multifunctional, and wearable electronics based on MXene-coated textile for personal heating systems, electromagnetic interference shielding, and pressure sensing. *J. Colloid Interface Sci.* 630, 23–33. <https://doi.org/10.1016/j.jcis.2022.09.003>.
52. Huang, A., Yang, Z., Zhu, Y., Tan, B., Song, Y., Guo, Y., Liu, T., and Peng, X. (2023). A unique, flexible, and porous pressure sensor with enhanced sensitivity and durability by synergy of surface microstructure and supercritical fluid foaming. *Appl. Surf. Sci.* 618, 156661. <https://doi.org/10.1016/j.apsusc.2023.156661>.
53. Huang, C.Y., Yang, G., Huang, P., Hu, J.M., Tang, Z.H., Li, Y.Q., and Fu, S.Y. (2023). Flexible pressure sensor with an excellent linear response in a broad detection range for human motion monitoring. *ACS Appl. Mater. Interfaces* 15, 3476–3485. <https://doi.org/10.1021/acsami.2c19465>.
54. Wang, F., Su, D., Ma, K., Qin, B., Li, B., Li, J., Zhang, C., Xin, Y., Huang, Z., Yang, W., et al. (2023). Reliable and scalable piezoresistive sensors with an MXene/MoS₂ hierarchical nanostructure for health signals monitoring. *ACS Appl. Mater. Interfaces* 15, 44001–44011. <https://doi.org/10.1021/acsami.3c09464>.
55. Jiang, H., Qin, M., Zhang, C., Weng, Z., Zhang, J., and Weng, X. (2023). Mixed-dimensional MXene nanocomposites/aramid nanofibers-based flexible pressure and strain sensor for electronic skin. *ACS Appl. Electron. Mater.* 5, 2276–2287. <https://doi.org/10.1021/acsaelm.3c00113>.
56. Qi, Z., Zhang, T., Zhang, X.D., Xu, Q., Cao, K., and Chen, R. (2023). MXene-based flexible pressure sensor with piezoresistive properties significantly enhanced by atomic layer infiltration. *Nano Mater. Sci.* 5, 439–446. <https://doi.org/10.1016/j.nanoms.2022.10.003>.
57. Yang, N., Liu, H., Yin, X., Wang, F., Yan, X., Zhang, X., and Cheng, T. (2022). Flexible pressure sensor decorated with MXene and reduced graphene oxide composites for motion detection, information transmission, and pressure sensing performance. *ACS Appl. Mater. Interfaces* 14, 45978–45987. <https://doi.org/10.1021/acsami.2c16028>.
58. Chen, T., Yang, G., Li, Y., Li, Z., Ma, L., Yang, S., and Wang, J. (2022). Temperature-adaptable pressure sensors based on MXene-coated GO hierarchical aerogels with superb detection capability. *Carbon* 200, 47–55. <https://doi.org/10.1016/j.carbon.2022.08.002>.
59. Zhu, B., Xu, Z., Liu, X., Wang, Z., Zhang, Y., Chen, Q., Teh, K.S., Zheng, J., Du, X., and Wu, D. (2023). High-linearity flexible pressure sensor based on the gaussian-curve-shaped microstructure for human physiological signal monitoring. *ACS Sens.* 8, 3127–3135. <https://doi.org/10.1021/acssensors.3c00818>.
60. Chen, B., Zhang, L., Li, H., Lai, X., and Zeng, X. (2022). Skin-inspired flexible and high-performance MXene@polydimethylsiloxane piezoresistive pressure sensor for human motion detection. *J. Colloid Interface Sci.* 617, 478–488. <https://doi.org/10.1016/j.jcis.2022.03.013>.
61. Wang, G., Liu, X., Song, Z., Yu, D., Li, G., Wang, H., Ge, S., and Liu, W. (2023). Multifunctional flexible pressure sensor based on a cellulose fiber-derived hierarchical carbon aerogel. *ACS Appl. Electron. Mater.* 5, 1581–1591. <https://doi.org/10.1021/acsaelm.2c01628>.
62. Cui, X., Jiang, Y., Hu, L., Cao, M., Xie, H., Zhang, X., Huang, F., Xu, Z., and Zhu, Y. (2023). Synergistically microstructured flexible pressure sensors with high sensitivity and ultrawide linear range for full-range human physiological monitoring. *Adv. Mater. Technol.* 8, 2200609. <https://doi.org/10.1002/admt.202200609>.
63. Yu, Q., Su, C., Bi, S., Huang, Y., Li, J., Shao, H., Jiang, J., and Chen, N. (2022). Ti₃C₂T_x@nonwoven fabric composite: promising MXene-coated fabric for wearable piezoresistive pressure sensors. *ACS Appl. Mater. Interfaces* 14, 9632–9643. <https://doi.org/10.1021/acsami.2c00980>.
64. Shi, L., Li, Z., Chen, M., Zhu, T., and Wu, L. (2023). Ultrasensitive and ultraprecise pressure sensors for soft systems. *Adv. Mater.* 35, 2210091. <https://doi.org/10.1002/adma.202210091>.
65. Ha, K.H., Zhang, W., Jang, H., Kang, S., Wang, L., Tan, P., Hwang, H., and Lu, N. (2021). Highly sensitive capacitive pressure sensors over a wide pressure range enabled by the hybrid responses of a highly porous nanocomposite. *Adv. Mater.* 33, 2103320. <https://doi.org/10.1002/adma.202103320>.
66. Zheng, X., Zhang, S., Zhou, M., Lu, H., Guo, S., Zhang, Y., Li, C., and Tan, S.C. (2023). MXene functionalized, highly breathable and sensitive pressure sensors with multi-layered porous structure. *Adv. Funct. Mater.* 33, 2214880. <https://doi.org/10.1002/adfm.202214880>.
67. He, J., Xiao, P., Lu, W., Shi, J., Zhang, L., Liang, Y., Pan, C., Kuo, S.W., and Chen, T. (2019). A Universal high accuracy wearable pulse monitoring system via high sensitivity and large linearity graphene pressure sensor. *Nano Energy* 59, 422–433. <https://doi.org/10.1016/j.nanoen.2019.02.036>.
68. Liu, J., Wang, H., Liu, T., Wu, Q., Ding, Y., Ou, R., Guo, C., Liu, Z., and Wang, Q. (2022). Multimodal hydrogel-based respiratory monitoring system for diagnosing obstructive sleep apnea syndrome. *Adv. Funct. Mater.* 32, 2204686. <https://doi.org/10.1002/adfm.202204686>.